



RESEARCH ARTICLE

10.1029/2022WR033304

Key Points:

- Incoming river flow to Yesa reservoir dwindled as vegetation cover increased
- Inter-annual time-scales increased their control of the annual discharge
- The is a growing influence of Mediterranean atmospheric dynamics on the river flow discharge

Correspondence to:

C. Juez,
carmelo.juez@ipe.csic.es

Citation:

Juez, C., Garijo, N., Vicente-Serrano, S. M., & Beguería, S. (2023). Six decades of hindsight into Yesa reservoir (Central Spanish Pyrenees): River flow dwindles as vegetation cover increases and Mediterranean atmospheric dynamics take control. *Water Resources Research*, 59, e2022WR033304. <https://doi.org/10.1029/2022WR033304>

Received 21 JUL 2022
Accepted 18 DEC 2022


Author Contributions:

Conceptualization: C. Juez, S. Beguería
Data curation: C. Juez, N. Garijo, S. M. Vicente-Serrano
Formal analysis: C. Juez, N. Garijo, S. M. Vicente-Serrano, S. Beguería
Methodology: C. Juez, N. Garijo, S. Beguería
Validation: S. Beguería
Writing – original draft: C. Juez, N. Garijo, S. M. Vicente-Serrano, S. Beguería
Writing – review & editing: C. Juez, N. Garijo, S. M. Vicente-Serrano, S. Beguería

© 2022 The Authors.

This is an open access article under the terms of the [Creative Commons Attribution-NonCommercial License](https://creativecommons.org/licenses/by/4.0/), which permits use, distribution and reproduction in any medium, provided the original work is properly cited and is not used for commercial purposes.

Six Decades of Hindsight Into Yesa Reservoir (Central Spanish Pyrenees): River Flow Dwindles as Vegetation Cover Increases and Mediterranean Atmospheric Dynamics Take Control

C. Juez^{1,2} , N. Garijo³, S. M. Vicente-Serrano² , and S. Beguería¹

¹Estación Experimental de Aula Dei, Consejo Superior de Investigaciones Científicas (EEAD-CSIC), Zaragoza, Spain, ²Instituto Pirenaico de Ecología, Consejo Superior de Investigaciones Científicas (IPE-CSIC), Zaragoza, Spain, ³Universidad de Valladolid, Campus Universitario Duques de Soria, Soria, Spain

Abstract River discharge has experienced diverse changes in the last decades due to modification of hydrological patterns, anthropogenic intervention, re-vegetation or annual and interannual climatic and atmospheric fluctuations. Assessing the recent changes in river discharge and understanding the main drivers of these changes is thus extremely important from theoretical and applied points of view. More specifically, here we want to draw attention toward the impacts of streamflow changes on reservoir storage and operation. We describe the hydrological dynamics of the Yesa reservoir draining catchment, located in the central Spanish Pyrenees, and characterize the reservoir operation modes over the last 60 years (1956–2020). We analyze concurrent climatic (precipitation, air temperature, drought index), atmospheric mechanisms, land cover (Normalized Different Vegetation Index) and discharge (inlet and outlet of Yesa reservoir) time-series. By using the wavelet transform methodology, we detect historical breakpoints in the hydrological dynamics at different time-scales. Distinctive periods are thus identified. More regular seasonal flows characterized the catchment's dynamics during the first decades of the study period, while the last decades were characterized by a high inter-annual variability. These changes are primarily attributed to the natural re-vegetation process that the catchment experienced. Furthermore, we related changes in atmospheric circulation with a decline of the long-term discharge temporal features. This research contributes to the understanding of long-term river discharge changes and helps to improve the reservoir management practices.

1. Introduction

River discharge characterization plays a fundamental role on a broad framework of fields: (a) flood control, as the magnitude and frequency of discharge levels are relevant to mitigate the impacts of floods (Lorenzo-Lacruz et al., 2022); (b) lotic system, since changes in river water supply strongly impact the species populating the river (Biggs et al., 2005); and (c) reservoir control, because changes in discharge levels and variability determine the operational activity of reservoirs (Schleiss et al., 2016). Numerous research has been thus devoted to investigate river discharge dynamics on the basis of historical records. In particular, attention has been devoted to assessing long-term river discharge trends around the world. Probst and Tardy (1987) analyzed the annual discharge data of 50 major rivers around the world for the 1910–1975 period, and found that European and Asian discharge records experienced higher values during the first half of the study period due to a predominant humid regime. On the contrary, African, North and South American discharge records were affected by this humid regime during the last half of the study period. This divergence of discharge trends was attributed to pressure oscillations operating at different time-scales. Milliman et al. (2008) studied the cumulative annual discharge from 137 rivers across the world for the 1951–2000 period. They observed that mid-latitude rivers suffered a decline in discharge, while a number of high-latitude and high-altitude rivers experienced an increase. River discharge changes were attributed to changes in precipitation due to climatic fluctuations and to anthropogenic impacts (dam construction, irrigation, civil infrastructure protection). In Europe, river discharges show notably diverging trends, with increasing discharge in the north as a result of increasing precipitation and a significant decline in the south because of land cover changes (Morán-Tejada et al., 2012; Teuling et al., 2019) and an increase of the water demand for irrigation (Masseroni et al., 2021; Vicente-Serrano et al., 2019). Within Europe, river discharges in the Iberian Peninsula were thoroughly analyzed by Lorenzo-Lacruz et al. (2012). 187 sub-basins were studied for the period 1945–2005, looking for annual and seasonal trends. The results showed a marked decrease in annual, winter and spring river discharge in most of the Iberian basins, especially in the south. The authors attributed the decrease

in water yield to a generalized re-vegetation process as a result of land abandonment and the increase of human water demands given crop irrigation.

Based on this previous research we can state that river discharges are characterized by diverse changes in the last decades due to modification of hydrological patterns (Huntington, 2006; Zhang et al., 2011), anthropogenic intervention (Juez et al., 2021; Pérez-Ciria et al., 2019), re-vegetation (Forzieri et al., 2020; Vicente-Serrano et al., 2021) or annual and interannual climatic fluctuations (Labat, 2010; Lorenzo-Lacruz et al., 2022). All these changes can occur in a synchronous or asynchronous way, river discharge being the integrated response to all of them. Assessing the recent changes in river discharge and understanding the main drivers of these changes is thus extremely important from theoretical and applied points of view. More specifically, here we want to draw attention toward the impacts of streamflow changes on reservoir control. This is of particular interest given that reservoirs are essential for the water supply of human societies for human consumption, irrigation and energy production (Guillén-Ludeña et al., 2022; Schleiss et al., 2016). Reservoirs were often built and commissioned under river discharge conditions that are different from the current ones (Guillén-Ludeña et al., 2018). Furthermore, in the next decades, reservoirs will have to address the impact of climate change (Sen et al., 2021), new environmental regulations (to preserve and protect natural ecosystems, Yin et al., 2011), a likely increasing water demand (mostly due to higher irrigation demand to meet increasing food production needs, Wriedt et al., 2009) and ultimately, reservoirs will play a key role for energy transition toward renewable sources of electricity (Fry et al., 2022).

The main goal of this work consists of identifying and describing the hydrological dynamics of the Yesa reservoir's catchment in the Central Spanish Pyrenees and the reservoir operation, by using a long-term and relevant database collected over 60 years (1956–2020). The Yesa reservoir was built for irrigation purposes, and the draining catchment underwent a process of re-vegetation for the last decades (García-Ruiz et al., 2015). We make use of robust statistical tools such as the wavelet transform method, which is able to distinguish different time-scales of variability and localize changes in the modes of variability within time-series (Carey et al., 2013; Juez & Nadal-Romero, 2020, 2021; Juez et al., 2021; Labat et al., 2005; Pérez-Ciria et al., 2019; Restrepo et al., 2014). This is an important step forward in identifying changing patterns at different and non-similar time-scales, enabling explaining the causes of observed changes and understanding their implications (Zhang et al., 2011). We evaluate the impact of annual to decadal periodicities in the reservoir's input discharge and identify non-stationary connections with: (a) the dominant atmospheric circulation indices in the region (North Atlantic Oscillation Index (NAO) and Western Mediterranean Oscillation index). These atmospheric indices have been recently related to the modification of temporal periodicities in streamflow records (Lorenzo-Lacruz et al., 2022); (b) climatic forcings (precipitation, air temperature and drought index); and (c) trends in vegetation activity. Comparison between input and output discharge offers a deeper insight into the operational aspects of the reservoir. This review of the historical records provides valuable insights about how to best address future challenges and future management decisions.

2. The Upper Aragón Catchment and the Yesa Reservoir

The upper Aragón River catchment is located in the Central Spanish Pyrenees, and drains an area of 2,181 km² (Figure 1). The source of the Aragón River is located in the Astún Valley at an altitude of 2,600 m a.s.l. It flows north-south through the Canfranc valley and then turns to the west crossing the city of Jaca. After that it travels downstream until reaching the end of the catchment which coincides with the Yesa reservoir. In addition to the Aragón River, three other rivers drain water to the catchment: the Subordán, Veral, and Esca Rivers. The first two are tributaries of the Aragón River, while the Esca River conveys water into the reservoir close to its delta. All the rivers of the Upper Aragón catchment have a natural, unmanaged, regime up to the Yesa reservoir.

The Yesa reservoir was built to irrigate a surface of 81,000 ha located to the south of the catchment. Currently, it also supplies water to Zaragoza, the largest city (700,000 inhabitants) in the Ebro basin. The dam is 74 m high, and the reservoir has a water storage capacity of 450 Hm³. The reservoir is one of the largest in the Pyrenees, 14.7 km long and 2.4 wide, and it follows the east-to-west direction of the thalweg of the Aragón River. The reservoir received 600–700 Hm³/year on average in the last decade. The main water supply comes from the Aragón River (two thirds of the total), while the rest flows from the Esca River (one third of the total).

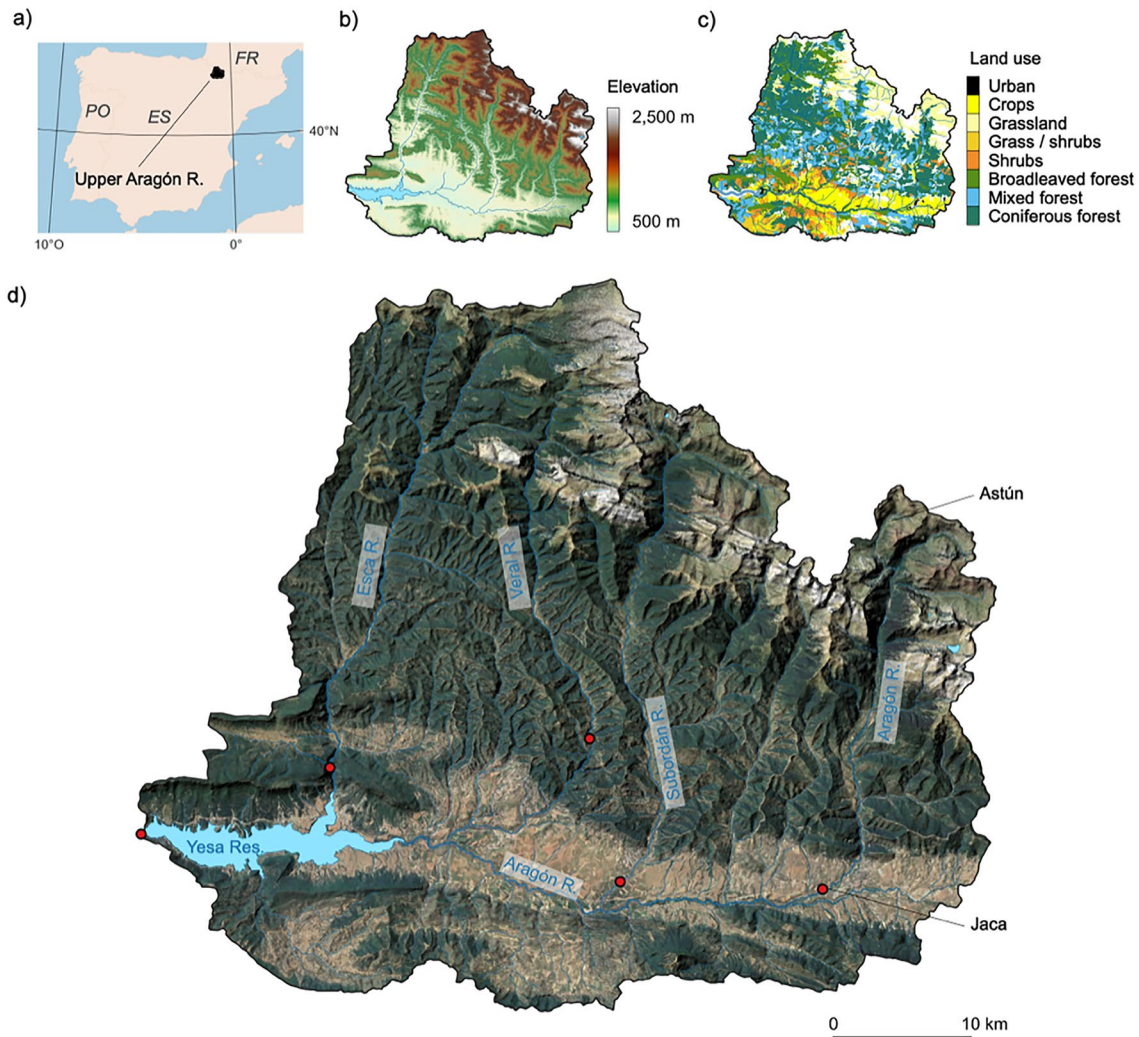


Figure 1. Location of the Upper Aragón River catchment (a), elevation (source: EUEDEM) (b), land use (source: CLC 2018), and general view of the study area with the main toponyms and location of the gauging stations (red points) used on this work (image source: Google).

The catchment area draining into the Yesa reservoir presents a complex lithology (containing areas with limestone, sandstone, clay and marls) and morphology (the altitude ranges between 2600 m a.s.l. in the northernmost area and 500 m a.s.l. at the Yesa reservoir). The long-term annual mean temperature (1956–2020) is 12°C. The mean annual precipitation in the catchment is approximately 860 mm, with a high inter-annual variability. Spring and autumn are the rainiest seasons. Summer is the driest season and it gets occasional storms due to convective processes.

Vegetation cover in the catchment was strongly impacted by human activities. Between 1950 and 1960 most of the cultivated fields were abandoned, with the exception of those located in the valley bottom. The abandoned fields, which represent around 25% of the catchment area, were colonized by shrubs and then trees, or reforested with pines (Lasanta et al., 2005; Vicente-Serrano et al., 2006).

3. Data and Methods

3.1. Air Temperature, Precipitation, Discharge, and Land Cover Data

Monthly precipitation and air temperature time-series records for the period 1956–2020 and for the Yesa reservoir were obtained from the Spanish National Meteorological Service (Agencia Estatal de Meteorología, AEMET). Further details about the processing methodology of this data set can be found in Vicente-Serrano et al., 2017.

Table 1
Temporal Breakpoints Detected by Wavelet Change-point Detection Analysis

Time-series	Wavelet change detection
Q Inlet	1977 (4-year, 8-year)
	1988 (8-year, 16-year, 32-year)
Q Outlet	1977 (4-year, 8-year)
	1988 (8-year, 16-year, 32-year)

Note. The year in which the change point was detected is displayed. The temporal scale associated to this breakpoint is shown in brackets.

Monthly discharge time-series data were obtained from the Ebro Water Authority (CHE), <http://www.chebro.es/>. The time series correspond to the inlet (adding together the contributions of the Aragón, Subordán, Veral and Esca Rivers and the outlet of the Yesa reservoir, covering 1956–2020 (Figure 1). Water level is measured routinely at these locations by CHE through the float method and water level probes, and daily discharge is computed afterward using rating curves. We did not have access to water level data, but used the computed discharge.

Land use and land cover maps at a spatial scale of 1:50,000 and for the decades of 1960s and 2010s were provided by the Spanish Ministry of Agriculture (see Figure 1 and Table 1). Furthermore, the Normalized Different Vegetation Index (NDVI) was used to obtain continuous annual time series of vegetation greenness of standing vegetation. The NDVI was calculated at

a spatial resolution of 1.1 km using the NOAA-AVHRR images covering the period 1982–2015 (Vicente-Serrano et al., 2020), combined with MODIS NDVI (Huete et al., 2002) for the period 2000–2020. Both data sets were standardized using the reference period 2000–2015 in order to provide homogeneous series that are not affected by the change of satellites.

3.2. Standardized Atmospheric Circulation and Drought Indices

Previous research has shown that the long-term variability of rainfall and river discharge time series can be explained by coupled modes of atmospheric circulation indices. The two main atmospheric circulation patterns that affect the western Mediterranean catchments are the NAO (Hurrell, 1995; Jones et al., 1997), and the Western Mediterranean Oscillation Index, WeMO (Angulo-Martínez & Beguería, 2012; Martín-Vide, 2006).

The NAO index is calculated as the normalized difference of pressure fields between Iceland and the Azores islands. The positive phase of the NAO refers to above-normal pressures over the Azores and below-normal pressures over Iceland causing mostly west-to-east circulation, while the negative phase indicates a high pressure pattern in the northeast Atlantic and more meridional circulation than the positive pattern. Positive phases of the NAO favors warmer and wetter winters in northern Europe and drier conditions in the south-western regions of Europe. The NAO index was already found responsible for precipitation and river discharge variability in the Iberian Peninsula (Lorenzo-Lacruz et al., 2012; Trigo et al., 2004).

The WeMO index is calculated as the normalized difference of pressure fields between the Liguria Gulf in Padua, in the north of Italy, and Cádiz, in the south of Spain. The positive phase of the WeMO index corresponds to the anticyclone over the Azores and low-pressures in the Liguria Gulf, and is often related to above-average precipitation in the north and northeast of the Iberian Peninsula (Martín-Vide, 2006). The negative phase of the WeMO index is linked with a central European anticyclone in the north of Italy and a low-pressure center in the south-west of the Iberian Peninsula. During WeMO negative phases wetter situations are recorded in the eastern areas of the Iberian Peninsula (Martín-Vide & Lopez-Bustins, 2006; Millán et al., 2005).

In addition to the monthly NAO and WeMO atmospheric indices we also used the monthly Standardized Precipitation Evapotranspiration Index (SPEI), which is a climatic drought index that enables identification of drought severity on different time-scales (Beguería et al., 2014; Vicente-Serrano et al., 2010). The SPEI is calculated based on the climatic water balance (i.e., the difference between precipitation and atmospheric evaporative demand), and the resulting values are fit to a log-logistic probability distribution to transform the original values into standardized units. The climatic water balance can be calculated at various time-scales (i.e., over 1 month, 2 months, etc.). Given the temporal inter-annual analysis herein purposed, and after assessing several time-scales, we used the SPEI data computed over 12-month. SPEI positive values refer to wetter-than-normal conditions, while negative values refer to dry conditions.

3.3. Wavelet Analysis

Hydroclimatic time-series are intrinsically non-stationary, and they integrate a broad set of transient patterns varying within the temporal record. The wavelet transform allows to localize in both time and periodicity the

transient patterns recorded in such non-stationary time-series. It thus provides a complete time-scale representation of localized and transient phenomena occurring at different time-scales (Torrence & Compo, 1998). In this research, we make use of the Morlet wavelet, which was successfully used in the past to analyze precipitation and discharge time-series (Carey et al., 2013; Juez & Nadal-Romero, 2021; Juez et al., 2021; Pérez-Ciria et al., 2019). This wavelet type is characterized as:

$$\varphi_0(\eta) = \pi^{-1/4} e^{i\omega_0\eta} e^{-\eta^2/2} \quad (1)$$

where $\varphi_0(\eta)$ is the wavelet function, η , is a dimensionless time parameter, i is the imaginary unit and ω_0 is the dimensionless angular frequency taken as 6 as it provides a good match between time and frequency localization.

Thus, the Continuous Wavelet Transform (CWT) for a time-series X_n , and for each scale s at all n of series length N , is mathematically represented as:

$$W_n(s) = \sum_{n'=0}^{N-1} x_{n'} \psi^* \left[\frac{(\eta' - \eta) \Delta t}{s} \right] \quad (2)$$

where $W_n(s)$ is the wavelet transform coefficients, ψ the normalized wavelet (the Morlet wavelet in our case), $(^*)$ the complex conjugate, s the wavelet scale, n the localized time index, and n' the translated time index of the time ordinate x . The CWT enables to plot a global picture showing the varying amplitude at each time-scale and along the time-line (Torrence & Compo, 1998).

In addition to the CWT we also used the discrete wavelet transform (DWT), which analyzes the time-series into increasing finer octave bands. These octave bands are normally based on integer powers of two (Tiwari & Adamowski, 2013). Thanks to the orthogonal temporal de-composition of the DWT analysis we can infer the temporal contribution of each time-scale. The discrete wavelet function is mathematically represented as:

$$\psi_{j,k}(t) = 2^{j/2} \psi(2^j t - k) \quad (3)$$

Breakpoints in the historical records were also identified by means of the wavelet change point analysis proposed by Percival and Walden (2000), and recently successfully applied by Pérez-Ciria et al. (2019). This technique finds breakpoints in the historical records by identifying changes in the variance of the time-series for each time-scale. We used a 95% confidence level for the test.

Finally, to complete the analysis, we studied the interaction between pairs of time-series by computing a bivariate framework called wavelet coherence (Grinsted et al., 2004), which compares two wavelet spectra corresponding to two time-series. The wavelet coherence measures the local linear correlation between two time-series, X and Y , with wavelet transforms $W_n^X(s)$ and $W_n^Y(s)$ at each time-scale. Hence, it is analogous to the squared correlation coefficient in linear regression. Because of these characteristics, the wavelet coherence can identify regions in the time space where the examined time-series co-move, but do not necessarily have a high common power. We compute the wavelet coherence coefficients following the approach of Grinsted et al. (2004):

$$R_n^2(s) = \frac{|\mathcal{S}(s^{-1} W_n^{XY}(s))|^2}{\mathcal{S}(s^{-1} |W_n^X(s)|^2) \cdot \mathcal{S}(s^{-1} |W_n^Y(s)|^2)} \quad (4)$$

being \mathcal{S} a smoothing operator for both scale and time domains:

$$\mathcal{S}(W) = \mathcal{S}_{\text{scale}}(\mathcal{S}_{\text{time}}(W_n(s))) \quad (5)$$

where $\mathcal{S}_{\text{time}}$ smooths along the time axis and $\mathcal{S}_{\text{scale}}$ smooths along the scale axis. Wavelet coherence ranges between 0 (no relationship) and 1 (linear relationship). The wavelet coherence phase difference is also computed to provide details on the oscillation (cycles) between two time-series (see Juez et al., 2022; Lee & Kim, 2019).

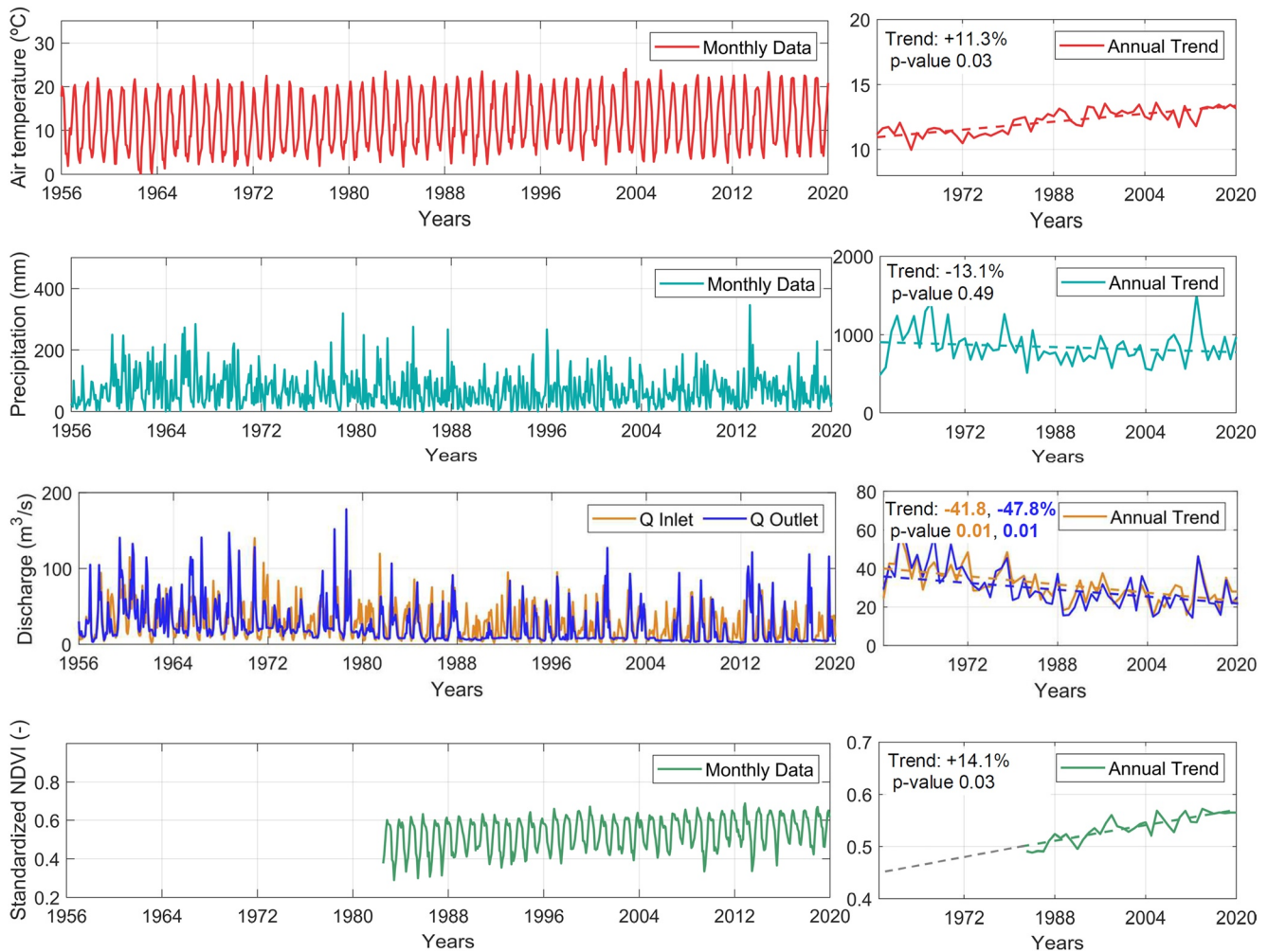


Figure 2. Time-series of monthly air temperature, precipitation, discharge at the inlet and outlet of Yesa reservoir and Normalized Different Vegetation Index (NDVI) records for the period 1956–2020 (left). Temporal evolution of annual air temperature, precipitation, discharge and NDVI records for the period 1956–2020. Dashed lines represent the linear trend obtained by means of least-squares. Percentage changes between 1956 and 2020 are obtained from the regression lines. P-values are obtained by means of the Mann-Kendall test. Gray dashed line in NDVI records illustrates the linear extrapolation for the non-data 1956–1982 period (right).

3.4. Trend Analysis

We used the Mann-Kendall test to assess decreasing or increasing trends over time for each data set and also to assess whether the resulting trend is statistically significant. Pre-whitening was used to eliminate the influence of serial correlation on the Mann-Kendall test, following the method proposed by Yue et al., 2002.

4. Results

4.1. Temporal Spectrum Dynamics

Monthly records of climatic forcings and river discharge are plotted and analyzed in Figure 2. Air temperature records display an important seasonal variability. A general rise in annual mean temperature is observed, statistically significant at the 95% level (p -value < 0.05), amounting to 11% over the whole study period (i.e., 1.2°C). Precipitation time-series show a bi-modal seasonal distribution with alternating dry (winter and summer) and wet (spring and autumn) seasons. Furthermore, precipitation exhibits a high interannual variability, and a non-significant decrease of 13% in the annual totals. River discharge at the inlet shows a high variability, with low flows during dry seasons and high flows during wet seasons. The highest discharges are found at the end of spring, when snowmelt coincides with high precipitation. At the outlet, the pattern of discharge is different due to

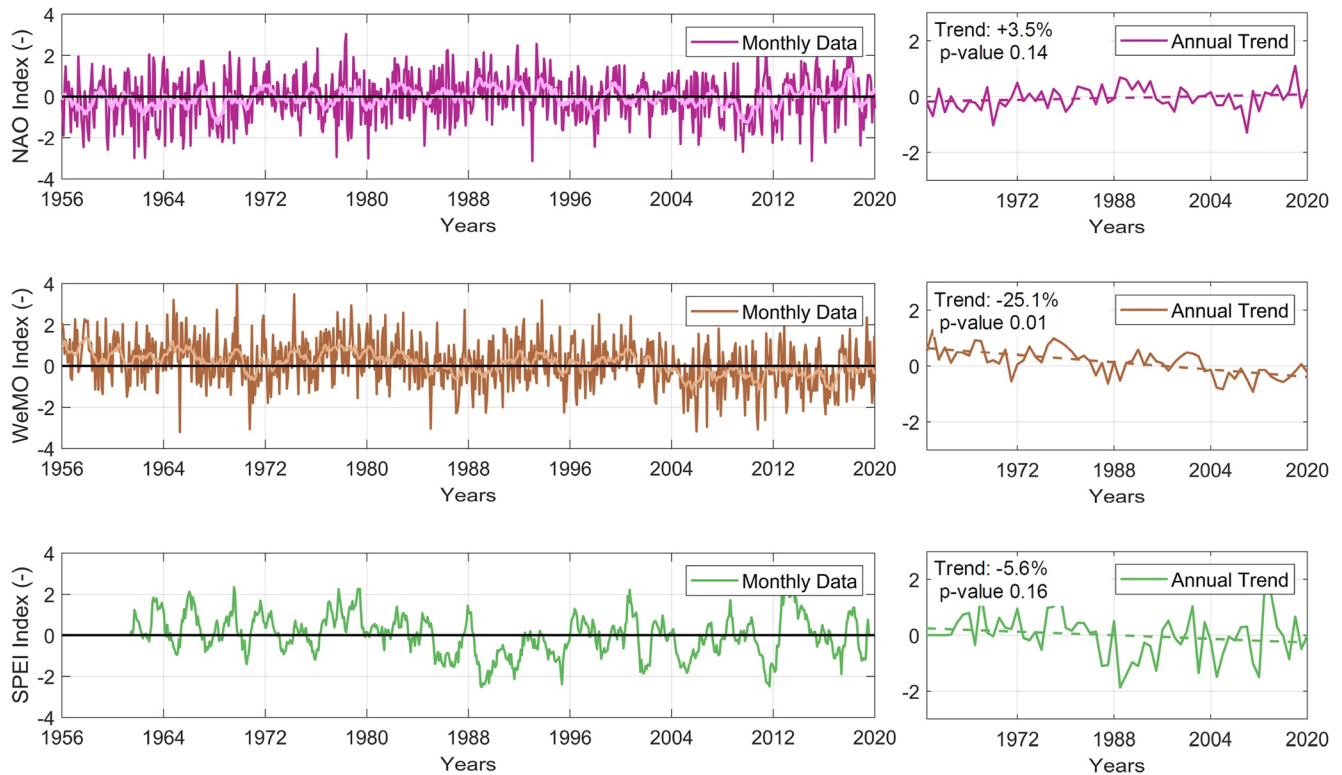


Figure 3. Time-series of monthly North Atlantic Oscillation Index (NAO), Western Mediterranean Oscillation Index (WeMO), and Standardized Precipitation Evapotranspiration Index (SPEI) (computed for 12-month time-scale) indices for the period 1956–2020. Light colors in NAO and WeMO correspond to a 12-month moving mean (left). Temporal evolution of annual NAO, WeMO, and SPEI records for the period 1956–2020. Dashed lines represent the linear trend obtained by means of least-squares. Percentage changes between 1956 and 2020 are obtained from the regression lines. *P*-values are obtained by means of the Mann-Kendall test (right).

the seasonal reservoir operation modes. Low outflows are recorded in autumn and spring, as most of the inflows are used to increase the water storage. In winter, a large part of the inlet discharge is released as a safety measure against spring floods. During summer a quasi-steady outflow is maintained to satisfy the high water demand. As a result, the outlet discharge is often higher (it very rarely drops below 10 m³/s) than the inlet discharge (which can reach 2 m³/s values) during summer. Both discharges, at the inlet and outlet, present a statistically significant decline of -41% and -47%, respectively. The temporal evolution of the NDVI is computed for the whole draining catchment and for the 1982–2020 period. Complete annual information before 1982 is not available, as the first NOAA-AVHRR satellite was launched in July 1981. NDVI shows a strong seasonal variation in vegetation dynamics. Increasing values are recorded during the vegetation-growing season (February–June). The intra-annual decline in NDVI values corresponds to the cold season (October–January). A consistent and statistically significant upward trend in vegetation greenness of 14% is found over the whole study period.

Figure 3 displays the temporal variability and analysis of NAO, WeMO, and SPEI indices. The NAO index shows a slight and non-statistically significant increase in its annual values. On the contrary, the WeMO index exhibits a statistically significant decrease of 25%. The SPEI index shows high temporal variability, which describes wet and dry periods. A slight and non-significant decline of 5% is observed.

Temporal dynamics of the climatic forces and discharges are further analyzed with the local wavelet power spectrum in Figure 4. Air temperature exhibits a maximum power at annual time-scales, as well as a quasi-continuous pattern at 0.5-year time-scale (Figure 4a). A 2–3 year fluctuation also appears from 1985 to 2015. Precipitation exhibits a strong intra-annual variability for time-scales below 0.5-year (Figure 4b). Furthermore, an intermittent 0.5-year and annual process is observed over the hydrological record. Such intermittency illustrates the high inter-annual irregularity of precipitation, with a succession of wet and dry years.

The interannual discharge fluctuations at the inlet exhibits concurrent oscillations below the 0.5-year time-scale (Figure 4c). The power values are higher during the first decades than in the last decades, which coincides with

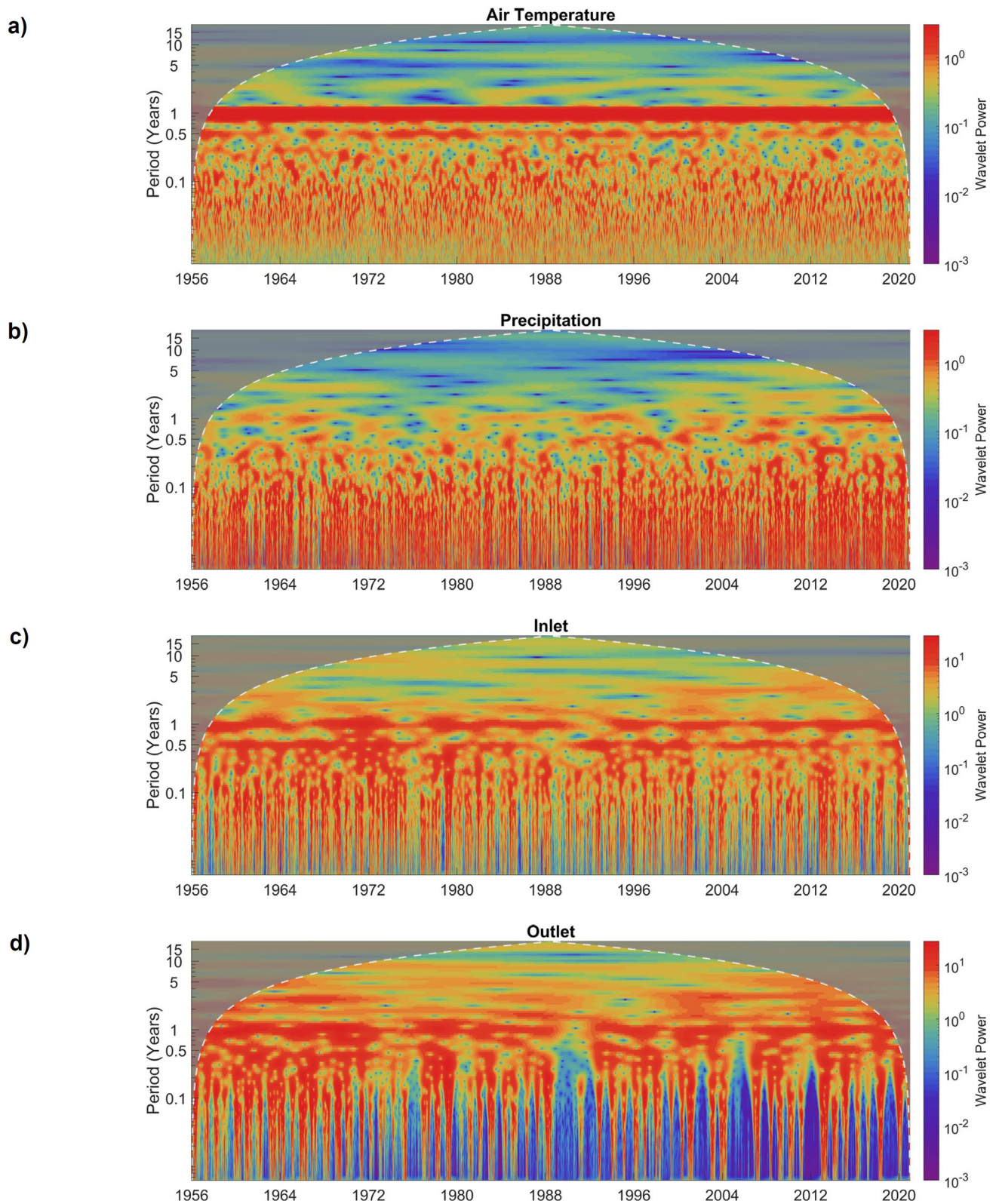


Figure 4. Local wavelet power spectrum of several time-series: air temperature (a), precipitation (b), discharge at the inlet (c), and discharge at the outlet (d). The vertical axis is the wavelet time-scale and the horizontal axis is the time position during the period 1956–2020 at Yesa reservoir. The dashed curve depicts the cone of influence below which the edge effects on the amplitude of the local power spectrum are negligible.

a decline in discharge. Furthermore, quasi-continuous 0.5-year and 1-year dynamics of comparable magnitude are identified. These processes coincide with those found for air temperature and precipitation. The 0.5-year oscillation allows to identify the hydrological cycle of the Upper Aragón catchment as a bi-modal cycle with high flow seasons (autumn and spring) and low flow seasons (winter and summer). The 1-year oscillation corresponds to the peak floods period which occurs once per year (during spring). Furthermore, a bi-annual fluctuation is identified during 1995–2018. A quasi-decadal oscillation (7–8 years) is also highlighted over the study period. Conversely, the interannual discharge fluctuations at the outlet display less variability at temporal scales below 0.5-year with regard to the inlet discharge (see Figure 4d). Furthermore, marked periods of low power values (blue colors) are periodically identified at intra-annual time-scales. These fluctuations conjugate with drought conditions identified thanks to the SPEI negative values (see Figure 3). Thus, under dry conditions the release of water from the reservoir is reduced at small temporal scales (>0.5-year) to ensure the water supply to the downstream region. These periods of dry conditions are intensified over the 1988–2020 interval (see negative values for the SPEI index in Figure 3), and they coincide with a decline of discharge records and with an intensification of low-power dynamics, both in terms of magnitude and recurrence (i.e., the discharge decline is intensified and dry conditions occur more often; see low wavelet power regions in Figure 4d). On the other hand, the wavelet spectrum highlights intervals of high intensity at 2–3 year time-scales between 1960–1972, 1982–1990, and 1998–2020. The quasi-decadal oscillation (7–8 years) previously observed at the inlet is also identified at the outlet over the study period.

Figure 5 displays the temporal decomposition of the historical records based on the DWT for long-term fluctuations which include 8-year, 16-year, and 32-year time-scales. The historical discharge time-series reflect a strong connection between the long-terms, and this temporal decomposition serves as a proxy to identify hydrological changes and varying hydrologic periodicities. This procedure was also applied to 2-year and 4-year time-scales, but these results are not shown here because they are not as relevant for the long-term connections.

The 8-year discharge component is characterized by higher fluctuations during the first decades, 1956–1982, with regard to lower fluctuations prevailing during the 1982–2012 interval. Precipitation displays a quasi-uniform variability over the whole study period. The NAO index presents an intensification of the fluctuations by the end of the period. The WeMO index exhibits fluctuations in the same order of magnitude as the NAO, but an attenuation of these processes are found in the interval 2004–2020. The SPEI index displays longer alternating periods of positive and negative anomalies.

The 16-year discharge component displays a modulation of the fluctuation with minimum anomalies found at the end of the analysis period. Precipitation and NAO are in-phase for two distinct intervals: 1956–1972 and 2010–2020. WeMO and SPEI indices are in-phase for most of the study period, between 1956 and 2006.

Finally, the 32-year component reflects the general trend of each time-series. A pronounced discharge decline is noted at both the inlet and outlet discharges. Precipitation also shows a decline over the interval 1960–2004, and a subsequent increase. The NAO displays an alternating cycle of negative and positive anomalies. The WeMO fluctuation depicts a downward trend from 1970 to 2013, with a pronounced decline within the interval 1996–2005. The SPEI displays an alternating cycle of negative and positive anomalies, but a general downward trend prevails.

4.2. Breakpoints in the Historical Records

Table 1 contains the summary of the historical breakpoints detected by the wavelet changepoint detection analysis at the inlet and outlet of the Yesa reservoir. Three intervals are distinguished: a first interval from 1956 to 1977, where changes in 4-year and 8-year time-scales are detected; a second interval after 1977–1988 which could be seen as a transition stage until a new discharge regime is achieved; and a third interval from 1988 to 2020, where a change in a wide spectrum of long-term time-scales is found (8-year, 16-year, and 32-year).

Relative cumulative discharge values at the inlet and at outlet, resulting from integrating the contribution of the different characteristic time-scales, are displayed in Figures 6 and 7, respectively. Results are displayed per year to show the intrinsic annual variability of each time scale. We also computed the discrete probability density of the cumulative discharge for the three temporal intervals identified in Table 1. Mean and standard deviation values are calculated for each interval. We used the standard deviation as a proxy to measure the magnitude of the anomalies in relation to the mean values of each interval.



Figure 5. 8-year, 16-year, and 32-year time-scale wavelet decomposition of six time-series recorded at Yesa reservoir for the period 1956–2020. Discharge at the inlet, discharge at the outlet, precipitation, North Atlantic Oceanic index, Western Mediterranean Oscillation index, and Standardized Precipitation Evapotranspiration Index index anomalies were calculated with respect to the mean values.



Figure 6. Comparison of cumulative discharge per year at the inlet of Yesa reservoir. Results are disaggregated in four temporal band-widths: 1-year, 1–4 years, 4–8 years, and 8–32 years (top). Discrete probability density function of the cumulative discharge disaggregated in the four temporal band-widths and for the three temporal breakpoint intervals identified (bottom).

As shown in Figure 6-top, the discharge supplied to the reservoir is mainly conveyed by the intra-annual fluctuations, and represents on average close to the 50% of the cumulative annual discharge. The remaining 50% is supplied by the 1–4-year time-scales (30% on average), the 4–8-year time-scale (10% on average), and the 8–32-year time time-scales (10% on average). On the other hand, differences are found among the three intervals identified. The discharge contribution of the intra-annual time-scales is reduced between the first and last intervals (mean values decline from 52% to 46%). Furthermore, the standard deviation is higher during the last interval. This implies a higher variability in the contribution of the intra-annual time-scales to the cumulative discharge per year. The discharge contribution of the 1–4-year time-scales is increased in the third interval, with regard to the first one (mean values increase from 27% to 34%). Furthermore, the standard deviation is also increased. The discharge contribution of the 4–8-year time-scales as well as the standard deviation is increased in the last interval. Finally, the 8–32-year time-scales experienced a decline in both terms of annual contribution and standard deviation.

Discharge dynamics at the outlet follows similar trends among intervals with regard to inlet discharge dynamics (see Figure 7). Discharge contribution by intra-annual time-scales constitutes the preponderant process in Yesa

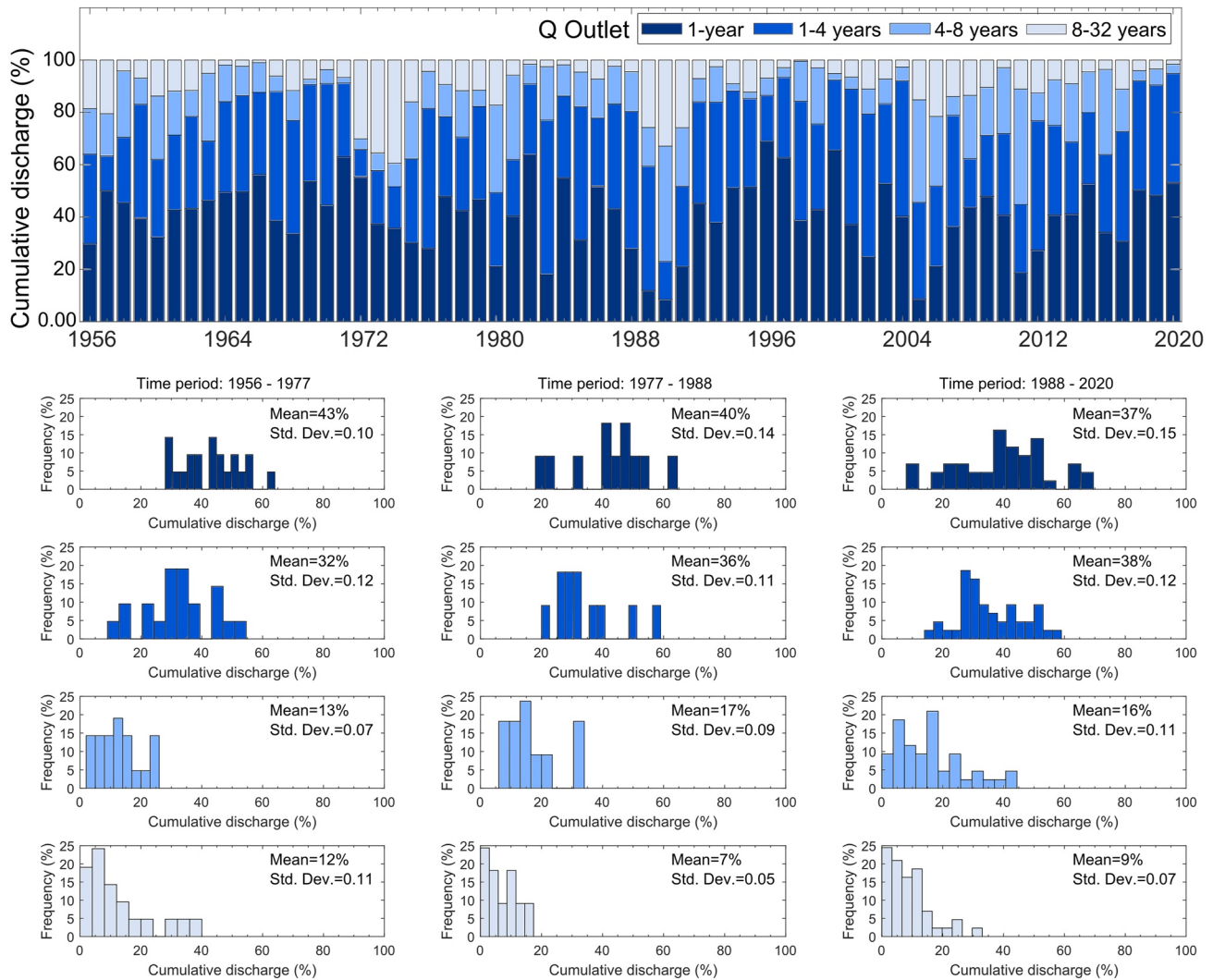


Figure 7. Comparison of cumulative discharge per year at the outlet of Yesa reservoir. Results are disaggregated in four temporal band-widths: 1-year, 1–4 years, 4–8 years, and 8–32 years (top). Discrete probability density function of the cumulative discharge disaggregated in the four temporal band-widths and for the three temporal breakpoint periods identified (bottom).

outlet discharge (mean values 40%). Furthermore, greater significance in discharge contribution is observed for the 1–4-year and 4–8-year time-scales during the last interval with regard to the first one.

4.3. Coupling Between Discharge and NAO, WeMO, and SPEI

The results of wavelet coherence between discharges and NAO, WeMO, and SPEI indices are shown in Figure 8. This analysis reveals the inter-annual and inter-decadal variability related to external climatic forces (Figure 9).

The wavelet coherence between discharge at the inlet and at the outlet of Yesa reservoir and NAO, WeMO, and SPEI indices displays weak wavelet coherence for time-scales below 0.5 year. This is not surprising, since time-shifts for discharge and atmospheric indices at such short time-scales are influenced by local orography, air temperature, precipitation intensity and areal distribution, resulting runoff amount and rate and floodwater travel rates. In other words, the climatic forces are controlling the time-shifts at such short time-scales. On the other hand, the discharge inter-annual variability fluctuations exhibit a stronger coupling with the NAO, WeMO, and SPEI indices at larger time-scales.

Discharge and NAO wavelet coherence reflects a global low value. Significant wavelet coherence values are found at annual and bi-annual scales, but with an intermittent pattern. Left oriented arrows in the figure indicate

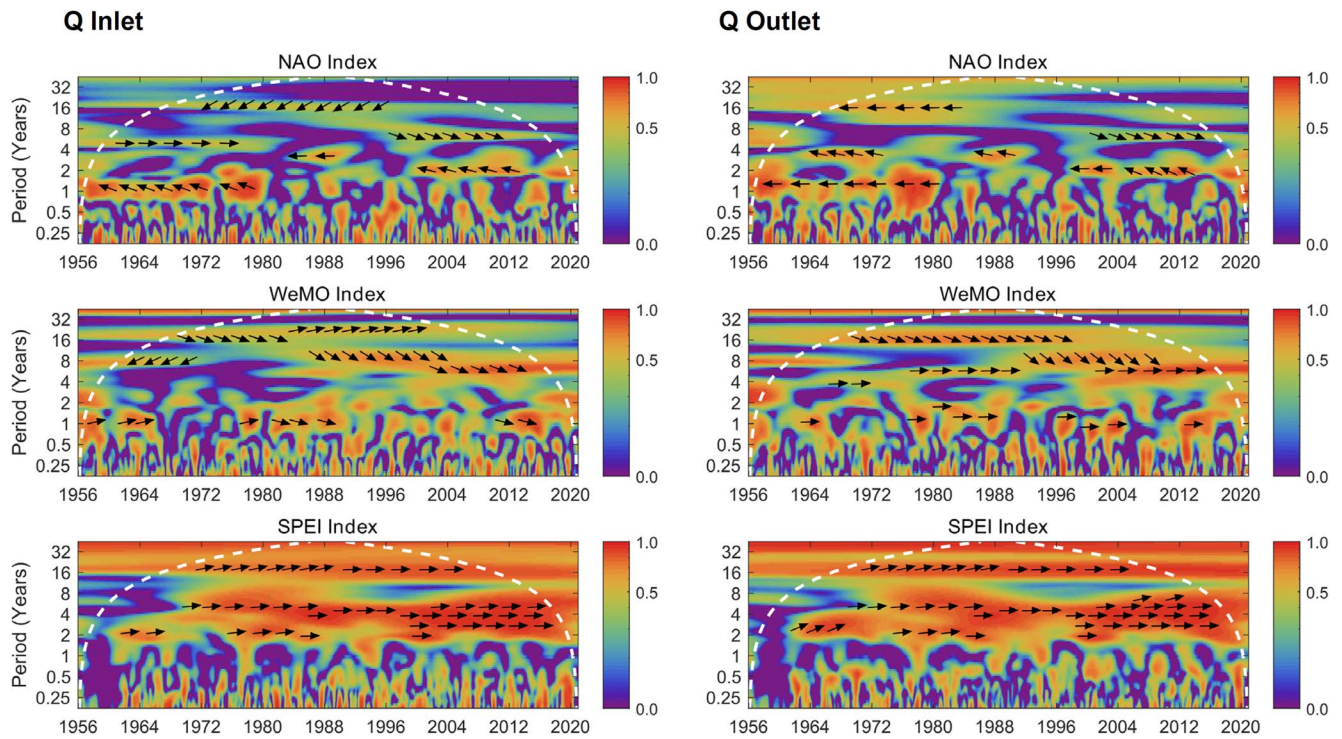


Figure 8. Squared wavelet coherence between monthly discharge and North Atlantic Oscillation Index, Western Mediterranean Oscillation Index, and Standardized Precipitation Evapotranspiration Index indices for the period 1956–2020 at the inlet (left) and at the outlet (right) of Yesa reservoir. The vertical axis is the time-scale and the horizontal line is the time position. The dashed curve depicts the cone of influence within which the edge effects are negligible. The shaded contours indicate the strength of the coherence. Wavelet coherence ranges between 0 (no relationship) and 1 (linear relationship). Arrows are plotted for time-scales above 0.5 year and in those regions where coherence is significant above the 0.6 level. Directions of the arrows indicate the degree to which discharge and standardized indices are in phase or have a time delay, that is, the arrows serve to identify the coupling between the two signals. Right arrows indicate discharge and standardized indices are in phase (0°), left arrows indicate discharge and standardized indices are completely out of phase (180°). An arrow pointing vertically upward (90°) means discharge peaks before standardized indices by one fourth of the cycle at that time-scale. An arrow pointing vertically downwards (phase angle of -90° or 270°) means discharge lags standardized indices by one fourth of the cycle at that time-scale.

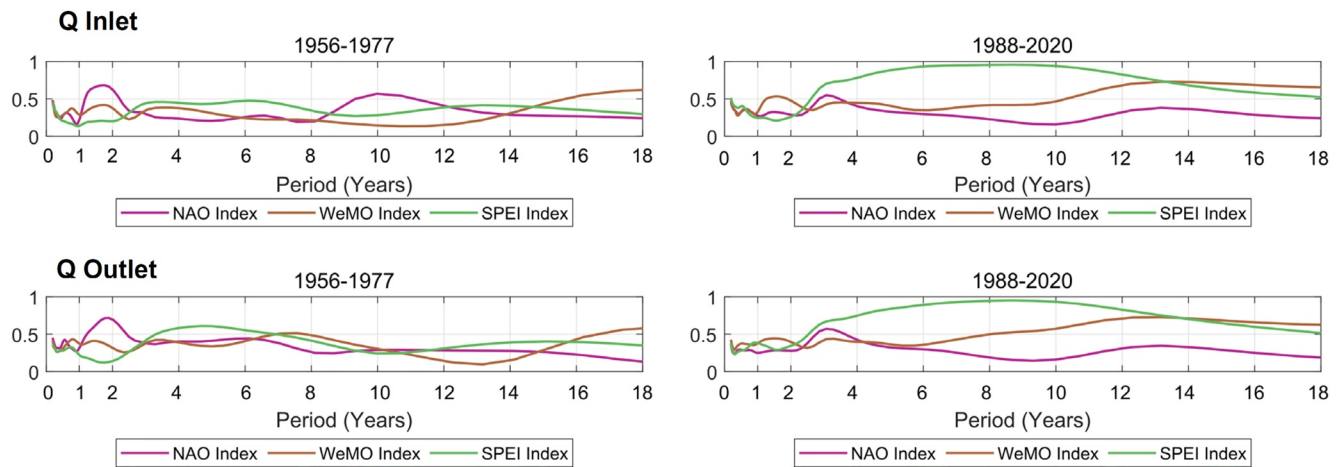


Figure 9. Time-averaged wavelet coherence between the monthly inlet discharge and North Atlantic Oscillation Index (NAO), Western Mediterranean Oscillation Index, and Standardized Precipitation Evapotranspiration Index (SPEI) anomalies (top) and between the monthly outlet discharge and NAO, WeMO, and SPEI anomalies (bottom) for the two largest distinct time-periods identified in Table 1. The horizontal axis corresponds to scales in years and the vertical axis corresponds to the wavelet coherence. Wavelet coherence ranges between 0 (no relationship) and 1 (linear relationship).

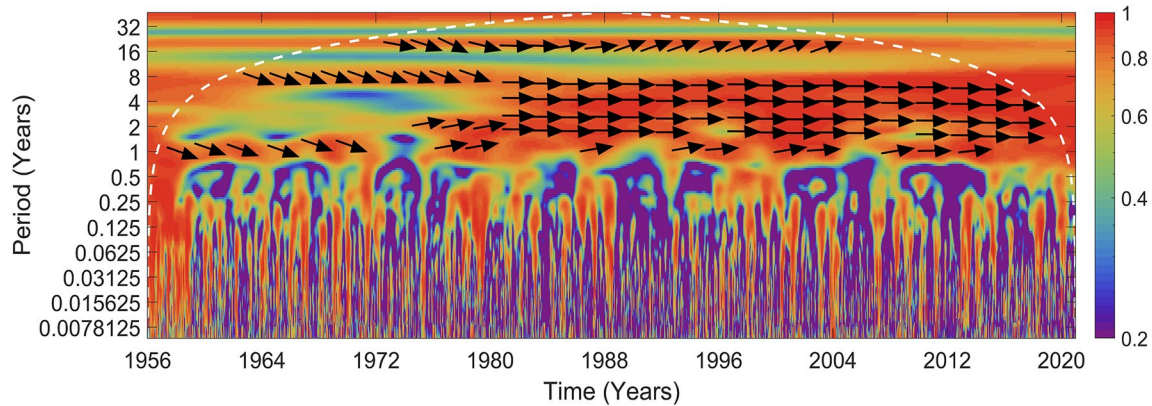


Figure 10. Squared wavelet coherence between discharge time-series for the period 1956–2020 at the inlet and at the outlet of Yesa reservoir. Wavelet coherence ranges between 0 (no relationship) and 1 (linear relationship). Arrows are plotted for time-scales above 0.5 year and in those regions where coherence is significant above the 0.6 level. Right arrows indicate discharge at the inlet and at the outlet are in phase (0°), left arrows indicate discharge at the inlet and at the outlet are completely out of phase (180°). An arrow pointing vertically upward (90°) means discharge at the inlet peaks before discharge at the outlet by one fourth of the cycle at that time-scale. An arrow pointing vertically downwards (phase angle of -90° or 270°) means discharge at the inlet lags discharge at the outlet by one fourth of the cycle at that time-scale.

that both time-series are out-of-phase for the inlet and outlet. Large-scale significant processes are also identified at 4-year and 16-year time-scales, although they are highly intermittent.

Discharge-WeMO wavelet coherence displays coherent large-scale coupling at time-scales larger than 4-year. A quasi-steady coupling over the whole study period is highlighted for the higher than 16-year time-scale. Strong wavelet coherence is also found over the 1985–2012 interval at the 8-year time-scale, and over the 2002–2018 interval at the 4-year time-scale. Arrows pointing downwards indicate that WeMO fluctuations peak before discharge at both inlet and outlet.

Concerning discharge and SPEI, strong wavelet coherence is found for concurrent large-scale processes at time-scales larger than 2-years, with the exception of two intervals at the 8-year time-scale: 1956–1972 and 1994–2012. Wavelet coherence values are intensified (wavelet coherence values above 0.9) during the interval 1997–2018.

We applied a time-averaging operator to the results displayed in Figure 8 in order to build a global estimator of wavelet coherence. Furthermore, we applied this time-averaging operator to the two largest distinct time-periods identified in Table 1 (i.e., we did not apply it to the interval 1977–1988 since it works as a transition period).

Regarding the interval 1956–1977 and the inlet discharge, the NAO index shows the largest values of wavelet coherence, more specifically at a bi-annual and quasi-decadal oscillation. At the outlet discharge the bi-annual signal is retrieved. However, the quasi-decadal process is not identified, which indicates that the reservoir operation is modulating the intensity of such long-term processes. Discharge-WeMO coupling reflects a general low value, regardless the time-scale. Discharge-SPEI values highlight a peak for the outlet and at 4–6-year time-scales.

The interval 1988–2020 displays similar values for both inlet and outlet discharge. Discharge-NAO values show low wavelet coherence for all the time-scales. On the contrary, there is an intensification of WeMO values, in particular for scales larger than 10-years, with regard to the previous interval. Discharge-SPEI wavelet coherence values highlight strong coupling for a wide range of time-scales (4–12-years).

4.4. Coupling Between Inlet and Outlet Discharge

In this section we explore the coupling between the discharge at the inlet and the outlet of Yesa reservoir by means of the wavelet coherence (see Figure 10). This coupling reflects the time-scale dependency between the water supplies to the reservoir (inlet) and the water supply downstream the reservoir (outlet).

The wavelet coherence for time-scales lower than 0.5-year displays global low values. Episodic and short intervals of high wavelet coherence values correspond to situations when the inlet discharge is released as a safety

measure against floods. At 0.5-year time-scales there is a succession of intervals with high and low wavelet coherence. These intervals are concomitant with drought periods identified with the SPEI index (see Figure 3). On the other hand, a near permanent coherence for annual processes is found but with changing dynamics. During 1956–1972, the arrows point downwards which indicate that inlet discharge lags outlet discharge, that is, as a safety measure water is released before receiving the annual peak flow. Furthermore, it is noted that between 1956 and 1960 the reservoir is impounded and it finally enters in commissioned at full capacity by 1960. From 1980, the right arrows reflect that both inlet and outlet are synchronized. Until 1980 at 8-year time-scale a strong wavelet coherence is found, and the arrows indicate that outlet discharge peaks before the inlet. From 1980, the 2–8-year wavelet coherence is high (>0.85), which indicates a linear relation between the timing when water is supplied to the river (inlet) and the water is supplied downstream (outlet). Furthermore, both time-series display right arrows, and thus a strong coupling. This coincides with the inlet discharge decline recorded over the last decades, which narrows the water availability and stresses the reservoir annual filling cycle. Finally, a strong coherence is observed for time-scales larger than 16-year over the whole study period and with distinct dynamics. Until 1980 the arrows point downwards. From 1980 onwards, the inlet and outlet discharge dynamics reveal a significant change with inlet discharge peaking before the outlet discharge. This behavior is similar to the one observed at 8-year time-scale.

5. Discussion

The analysis of concurrent long-term hydroclimatic time-series and atmospheric indices reveals the controlling physical processes of river discharge, which ultimately provide interesting insight on the past and forthcoming challenges for Yesa reservoir management. The first of these insights is that there is a severe and statistically significant decline in the magnitude of discharge measured at the inlet and at the outlet of the Yesa reservoir (about 40%). Furthermore, the scatter between both trends at the inlet and outlet is narrowed over the last decades. This implies that reservoir operators are focused on preserving as much water supplied to the reservoir as possible to be able to meet water demands downstream later in the season. Regulation operations give way to water storage operations, which become a priority.

Furthermore, the results indicate that this sharp decline in discharge cannot be attributed to a drop in precipitation, which shows a moderate and non-significant decline (about 10%, see Figure 2). Downwards discharge trends were already identified in other natural non-managed catchments in Spain (Lorenzo-Lacruz et al., 2012; Martínez-Fernández et al., 2013; Vicente-Serrano et al., 2020). These previous studies highlighted the link between the declining water yield and a process of general re-vegetation after generalized land abandonment. In the Upper Aragón catchment, the abandoned fields faced a greenness process in about 25% of the total catchment area (Vicente-Serrano et al., 2006). Furthermore, the upwards and statistically significant trend of NDVI values computed for the whole catchment from 1982 onwards confirms that re-vegetation continues to be a very relevant process in the area, and it can be hypothesized that it plays a major role in discharge decline due to increasing water consumption by vegetation. Further confirmation of vegetation impact on discharge decline is related with the temporal breakpoints identified. At shorter time-scales (4-years and 8-years) a temporal breakpoint was identified in 1977. This corresponds well with the intersection point identified in the discharge linear trends. As explained in Linscheid et al. (2020), those areas with shrublands and young trees (i.e., at the initial re-vegetation process faced by the catchment at early 1950) display NDVI values dominated by interannual trends, suggesting important roles in intra- and interannual biosphere dynamics of these land cover classes.

The second interesting insight arising from the results is that there is a reduction of the inlet cumulative discharge linked to the intra-annual timescales (up to 1-year, see Figure 6), which thus underlines the importance of the fluctuations linked to inter-annual time-scales. These long-term time-scales have the mission to recharge the water reserve of the catchment at a very general level (i.e., soils, aquifers, etc.), with a positive effect on the discharge. The decrease in the contribution of intra-annual time-scales over the study period can be due to three reasons. The first one is that the catchment experienced a moderate reduction in precipitation rates, which implies less resulting runoff. The second reason is that the sharp increase of vegetation in the catchment area lead to a larger water demand by plants at seasonal scales. As a result, vegetation cover dynamics dramatically reduced the annual production of runoff (Vicente-Serrano et al., 2021; Williams & Albertson, 2005). The relative contribution of inter-annual time-scales is thus increased. These findings suggest that precipitation and vegetation cover cause a water-limited state in the catchment. This trend seems to be accentuated in the last decades (see SPEI index in

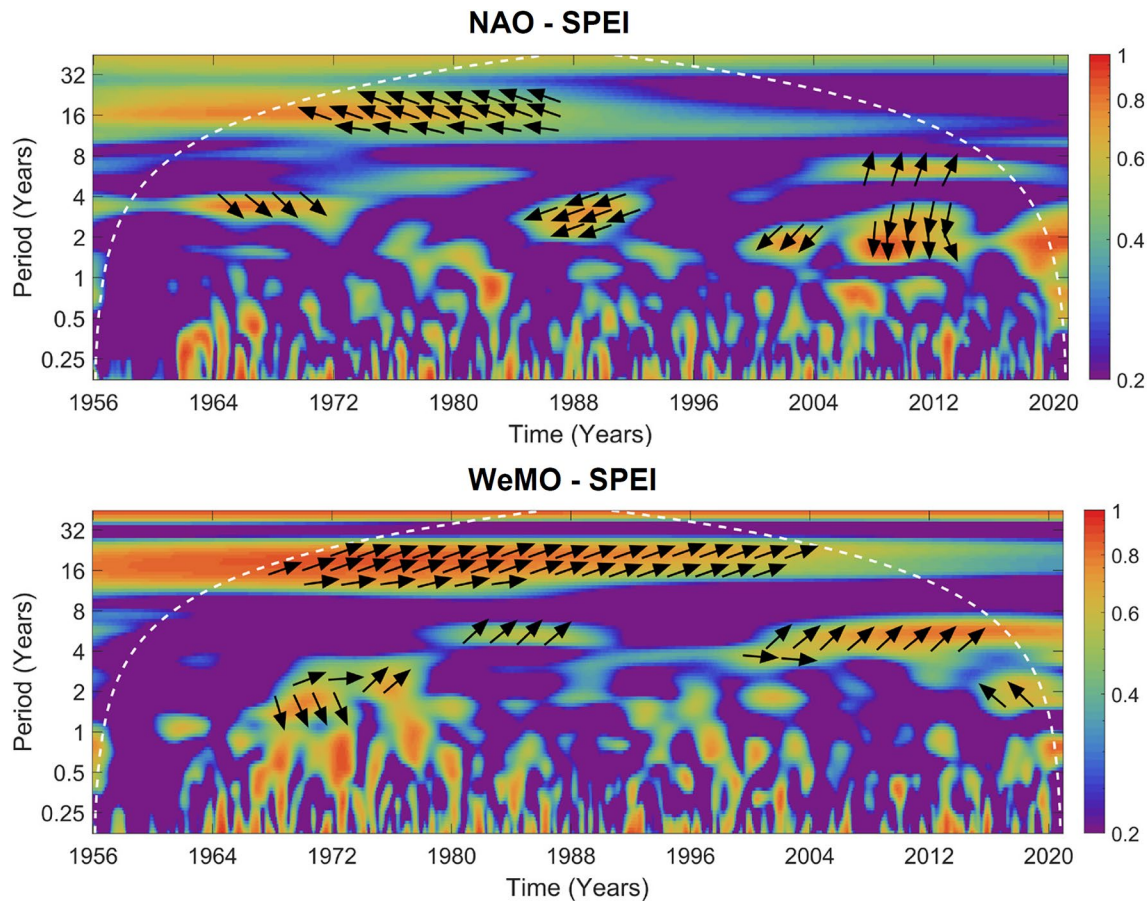


Figure 11. Squared wavelet coherence between North Atlantic Oscillation Index (NAO) and Standardized Precipitation Evapotranspiration Index (SPEI) indices (top) and between Western Mediterranean Oscillation Index (WeMO) and SPEI indices (bottom) for the period 1956–2020. Wavelet coherence ranges between 0 (no relationship) and 1 (linear relationship). Arrows are plotted for time-scales above 0.5 year and in those regions where coherence is significant above the 0.6 level. Right arrows indicate both indices are in phase (0°), left arrows indicate NAO or WeMO are completely out of phase with regard to SPEI (180°). An arrow pointing vertically upward (90°) means NAO or WeMO peaks before SPEI by one fourth of the cycle at that time-scale. An arrow pointing vertically downwards (phase angle of -90° or 270°) means NAO or WeMO lags SPEI by one fourth of the cycle at that time-scale.

Figure 2). The third reason is that the vegetation increase has reduced the visible and measurable discharge while it may have boosted the relative contribution of groundwater discharge. Tree root architecture enhances hydraulic redistribution of water in soils (Prieto et al., 2012), thus favoring groundwater discharge (Ilstedt et al., 2016).

The third insight is related with the atmospheric circulation patterns (NAO and WeMO) and the drought index (SPEI). NAO dynamics are well known to play a modulating role on the climatic variability in the North Atlantic, in particular during winter (Hurrell et al., 2003; Trigo et al., 2002). Negative NAO anomalies lead to increasing precipitation over most of the Iberian Peninsula. Nonetheless, the NAO role is reduced toward the east of the Iberian Peninsula because of the complex orography, which limits the arrival of humid weather fronts from the North Atlantic. In our results, the NAO index displays a relatively low relationship with the measured discharge (see Figure 8). On the contrary the WeMO index, which is modulated by Mediterranean atmospheric dynamics (López-Bustins et al., 2020; Martín-Vide & Lopez-Bustins, 2006), displays an increasing control on recorded discharge as illustrated in Figure 8. The relevance of the SPEI is also highlighted in Figure 8, in particular over the last decades, where an intensification of droughts is observed as consequence of the increase in the atmospheric evaporative demand (Domínguez-Castro et al., 2019). We computed the wavelet coherence between NAO and SPEI and between WeMO and SPEI (see Figure 11). NAO and SPEI indices show intermittent high coherence for time-scales smaller than 8-years. This is not surprising since the dominant quasi-decadal NAO mode, which modulates the positive and negative NAO anomalies, is a well-known dynamic (Hurrell et al., 2003). At larger time-scales there is a high coherence over the first decades which disappears after 1988. The WeMO and

SPEI indices display high coherence for decadal time-scales over the whole study period. At 4-year time-scale we also identified a high level of coherence for the 2000–2020 interval. We interpret this as an indicative of the growing influence of Mediterranean atmospheric dynamics with regards to the North Atlantic atmospheric dynamics.

The results and conclusions outlined in this study are complementary to those documented in the North Atlantic region, where the NAO is the dominant atmospheric mechanism (Hurrell & Dessler, 2009; Kingston et al., 2006; Lorenzo-Lacruz et al., 2022). In such studies, and in opposition to this study, it was showed a growing incidence of positive correlation between positive phases of the NAO and increasing discharge records in northeast France and the southern England all through the last two decades. Diverging spatial patterns of discharge records are thus identified between northern and southern Europe (the Central Spanish Pyrenees). This divergence in the trends of discharge dynamics has consequences for reservoir operation, which needs to be different depending on the local discharge fluctuations and as result of the existing dominant atmospheric mechanism.

6. Conclusions

By using the wavelet transform methodology, we detect historical breakpoints in the hydrological dynamics at different time-scales. As a result, the cross-interaction among different climatic, hydrologic and atmospheric dynamics are identified. We observed that the incoming river flow to Yesa Reservoir dwindled as vegetation cover increased in the catchment. Furthermore, inter-annual time-scales increased their control over the total annual discharge. Eventually, we also detected a growing influence of Mediterranean atmospheric dynamics on the river flow discharge control. We thus estimate that the decline observed in the annual mean discharge will continue in the following years, mainly driven by the projected NDVI increase, and also if the observed declining trend in the WeMO index persists, with a consequent decrease in precipitation. Projected Yesa reservoir management thus needs to take into account these insights because an increasing risk of severe water shortage is expected. The water demand downstream cannot be increased due to the increasing inter-annual variability of the annual discharge. Furthermore, this strong inter-annual variability stresses the reservoir capacity of satisfying current water demand during dry years.

Data Availability Statement

Data presented in this manuscript will be uploaded at an open repository if the paper is accepted for publication.

Acknowledgments

This work was partially funded by Fundación Biodiversidad under the project: *Evaluación de medidas de adaptación al cambio climático en la agricultura de regadío combinado predicciones de demanda de agua basadas en el comportamiento de los agricultores, condiciones hidro-climáticas y modelos de gestión* and by the Aragón Government and the European Social Fund (ESF-FSE) through the *Geoenvironmental Processes and Global Change* research group (E02_17E). C. J. also acknowledges funding from the European Research Council (ERC) through the Horizon Europe 2021 Starting Grant program under REA grant agreement number 101039181 - SED@HEAD.

References

- Angulo-Martínez, M., & Beguería, S. (2012). Do atmospheric teleconnection patterns influence rainfall erosivity? A study of NAO, MO and WeMO in NE Spain, 1955–2006. *Journal of Hydrology*, 450, 168–179. <https://doi.org/10.1016/j.jhydrol.2012.04.063>
- Beguería, S., Vicente-Serrano, S. M., Reig, F., & Latorre, B. (2014). Standardized precipitation evapotranspiration index (SPEI) revisited: Parameter fitting, evapotranspiration models, tools, data sets and drought monitoring. *International Journal of Climatology*, 34(10), 3001–3023. <https://doi.org/10.1002/joc.3887>
- Biggs, B. J., Nikora, V. I., & Snelder, T. H. (2005). Linking scales of flow variability to lotic ecosystem structure and function. *River Research and Applications*, 21(2-3), 283–298. <https://doi.org/10.1002/rra.847>
- Carey, S. K., Tetzlaff, D., Buttle, J., Laudon, H., McDonnell, J., McGuire, K., et al. (2013). Use of color maps and wavelet coherence to discern seasonal and interannual climate influences on streamflow variability in northern catchments. *Water Resources Research*, 49(10), 6194–6207. <https://doi.org/10.1002/wrcr.20469>
- Domínguez-Castro, F., Vicente-Serrano, S. M., Tomás-Burguera, M., Peña-Gallardo, M., Beguería, S., El Kenawy, A., et al. (2019). High spatial resolution climatology of drought events for Spain: 1961–2014. *International Journal of Climatology*, 39(13), 5046–5062. <https://doi.org/10.1002/joc.6126>
- Forzieri, G., Miralles, D. G., Ciais, P., Alkama, R., Ryu, Y., Duveiller, G., et al. (2020). Increased control of vegetation on global terrestrial energy fluxes. *Nature Climate Change*, 10(4), 356–362. <https://doi.org/10.1038/s41558-020-0717-0>
- Fry, J. J., Morris, M., & Schleiss, A. (2022). *Hydropower, a catalyst for energy transition in Europe*. LHB. 2058829.
- García-Ruiz, J. M., López-Moreno, J. I., Lasanta, T., Vicente-Serrano, S. M., González-Sampériz, P., Valero-Garcés, B. L., et al. (2015). Geocological effects of global change in the central Spanish Pyrenees: A review at different spatial and temporal scales. *Pirineos*, 170(0), e012. <https://doi.org/10.3989/Pirineos.2015.170005>
- Grinsted, A., Moore, J. C., & Jevrejeva, S. (2004). Application of the cross wavelet transform and wavelet coherence to geophysical time series. *Nonlinear Processes in Geophysics*, 11(5/6), 561–566. <https://doi.org/10.5194/npg-11-561-2004>
- Guillén-Ludeña, S., Manso, P. A., & Schleiss, A. J. (2018). Multidecadal sediment balance modelling of a cascade of alpine reservoirs and perspectives based on climate warming. *Water*, 10(12), 1759. <https://doi.org/10.3390/w10121759>
- Guillén-Ludeña, S., Toapaxi, J. A., & Castillo, L. G. (2022). Flushing capacity of a stored volume of water: An experimental study. *Water*, 14(17), 2607. <https://doi.org/10.3390/w14172607>

- Huete, A., Didan, K., Miura, T., Rodriguez, E. P., Gao, X., & Ferreira, L. G. (2002). Overview of the radiometric and biophysical performance of the MODIS vegetation indices. *Remote Sensing of Environment*, 83(1–2), 195–213. [https://doi.org/10.1016/S0034-4257\(02\)00096-2](https://doi.org/10.1016/S0034-4257(02)00096-2)
- Huntington, T. G. (2006). Evidence for intensification of the global water cycle: Review and synthesis. *Journal of Hydrology*, 319(1–4), 83–95. <https://doi.org/10.1016/j.jhydrol.2005.07.003>
- Hurrell, J. (1995). Decadal trends in North Atlantic Oscillation and relationship to regional temperature and precipitation. *Science*, 269(5224), 676–679. <https://doi.org/10.1126/science.269.5224.676>
- Hurrell, J. W., & Deser, C. (2009). North Atlantic climate variability: The role of the North Atlantic oscillation. *Journal of Marine Systems*, 78(1), 28–41. <https://doi.org/10.1016/j.jmarsys.2008.11.026>
- Hurrell, J. W., Kushnir, Y., Ottensen, G., & Visbeck, M. (2003). An overview of the North Atlantic oscillation. In *Geophysical monograph—American geophysical union* (Vol. 134, pp. 1–36).
- Istedt, U., Bargués Tobella, A., Bazić, H. R., Bayala, J., Verbeeten, E., Nyberg, G., et al. (2016). Intermediate tree cover can maximize ground-water recharge in the seasonally dry tropics. *Scientific Reports*, 6(1), 1–12. <https://doi.org/10.1038/srep21930>
- Jones, P. D., Jónsson, T., & Wheeler, D. (1997). Extension to the North Atlantic oscillation using early instrumental pressure observations from Gibraltar and South-West Iceland. *International Journal of Climatology*, 17(13), 1433–1450. [https://doi.org/10.1002/\(sici\)1097-0088\(199711\)17:13<1433::aid-joc203>3.0.co;2-p](https://doi.org/10.1002/(sici)1097-0088(199711)17:13<1433::aid-joc203>3.0.co;2-p)
- Juez, C., Garjito, N., Hassan, M. A., & Nadal-Romero, E. (2021). Intraseasonal-to-Interannual analysis of discharge and suspended sediment concentration time-series of the upper changjiang (Yangtze river). *Water Resources Research*, 57(8), e2020WR029457. <https://doi.org/10.1029/2020wr029457>
- Juez, C., Garjito, N., Nadal-Romero, E., & Vicente-Serrano, S. M. (2022). Wavelet analysis of hydro-climatic time-series and vegetation trends of the Upper Aragón catchment (Central Spanish Pyrenees). *Journal of Hydrology*, 614, 128584. <https://doi.org/10.1016/j.jhydrol.2022.128584>
- Juez, C., & Nadal-Romero, E. (2020). Long-term time-scale bonds between discharge regime and catchment specific landscape traits in the Spanish Pyrenees. *Environmental Research*, 191, 110158. <https://doi.org/10.1016/j.envres.2020.110158>
- Juez, C., & Nadal-Romero, E. (2021). Long-term temporal structure of catchment sediment response to precipitation in a humid mountain badland area. *Journal of Hydrology*, 597, 125723. <https://doi.org/10.1016/j.jhydrol.2020.125723>
- Kingston, D. G., Lawler, D. M., & McGregor, G. R. (2006). Linkages between atmospheric circulation, climate and streamflow in the northern North Atlantic: Research prospects. *Progress in Physical Geography*, 30(2), 143–174. <https://doi.org/10.1191/0309133306pp471ra>
- Labat, D. (2010). Cross wavelet analyses of annual continental freshwater discharge and selected climate indices. *Journal of Hydrology*, 385(1–4), 269–278. <https://doi.org/10.1016/j.jhydrol.2010.02.029>
- Labat, D., Ronchail, J., & Guyot, J. L. (2005). Recent advances in wavelet analyses: Part 2: Amazon, Parana, Orinoco and Congo discharges time scale variability. *Journal of Hydrology*, 314(1–4), 289–311. <https://doi.org/10.1016/j.jhydrol.2005.04.004>
- Lasanta, T., Vicente-Serrano, S., & Cuadrat, J. (2005). Mountain Mediterranean landscape evolution caused by the abandonment of traditional primary activities: A study of the Spanish central Pyrenees. *Applied Geography*, 25(1), 47–65. <https://doi.org/10.1016/j.apgeog.2004.11.001>
- Lee, E., & Kim, S. (2019). Wavelet analysis of soil moisture measurements for hillslope hydrological processes. *Journal of Hydrology*, 575, 82–93. <https://doi.org/10.1016/j.jhydrol.2019.05.023>
- Linscheid, N., Estupinan-Suarez, L. M., Brenning, A., Carvalhais, N., Cremer, F., Gans, F., et al. (2020). Towards a global understanding of vegetation–climate dynamics at multiple timescales. *Biogeosciences*, 17(4), 945–962. <https://doi.org/10.5194/bg-17-945-2020>
- López-Bustins, J. A., Arbiol-Roca, L., Martín-Vide, J., Barrera-Escoda, A., & Prohom, M. (2020). Intra-annual variability of the Western Mediterranean oscillation (WeMO) and occurrence of extreme torrential precipitation in catalonia (NE Iberia). *Natural Hazards and Earth System Sciences*, 20(9), 2483–2501. <https://doi.org/10.5194/nhess-20-2483-2020>
- Lorenzo-Lacruz, J., Morán-Tejeda, E., Vicente-Serrano, S. M., Hannaford, J., García, C., Peña-Angulo, D., & Murphy, C. (2022). Stream-flow frequency changes across Western Europe and interactions with North Atlantic atmospheric circulation patterns. *Global and Planetary Change*, 212, 103797. <https://doi.org/10.1016/j.gloplacha.2022.103797>
- Lorenzo-Lacruz, J., Vicente-Serrano, S. M., López-Moreno, J. I., González-Hidalgo, J. C., & Morán-Tejeda, E. (2012). The response of Iberian rivers to the North Atlantic oscillation. *Hydrology and Earth System Sciences*, 15(8), 2581–2597. <https://doi.org/10.5194/hess-15-2581-2011>
- Martínez-Fernández, J., Sánchez, N., & Herrero-Jiménez, C. M. (2013). Recent trends in rivers with near-natural flow regime: The case of the river headwaters in Spain. *Progress in Physical Geography*, 37(5), 685–700. <https://doi.org/10.1177/0309133313496834>
- Martín-Vide, J., & Lopez-Bustins, J. A. (2006). The Western Mediterranean oscillation and rainfall in the Iberian Peninsula. *International Journal of Climatology*, 26(11), 1455–1475. <https://doi.org/10.1002/joc.1388>
- Masseroni, D., Camici, S., Cislighi, A., Vacchiano, G., Massari, C., & Brocca, L. (2021). The 63-year changes in annual streamflow volumes across Europe with a focus on the Mediterranean basin. *Hydrology and Earth System Sciences*, 25(10), 5589–5601. <https://doi.org/10.5194/hess-25-5589-2021>
- Millán, M. M., Estrela, M. J., & Miró, J. (2005). Rainfall components: Variability and spatial distribution in a Mediterranean area (valencia region). *Journal of Climate*, 18(14), 2682–2705. <https://doi.org/10.1175/jcli3426.1>
- Milliman, J. D., Farnsworth, K. L., Jones, P. D., Xu, K. H., & Smith, L. C. (2008). Climatic and anthropogenic factors affecting river discharge to the global ocean, 1951–2000. *Global and Planetary Change*, 62(3–4), 187–194. <https://doi.org/10.1016/j.gloplacha.2008.03.001>
- Morán-Tejeda, E., Ceballos-Barbancho, A., Llorente-Pinto, J. M., & López-Moreno, J. I. (2012). Land-cover changes and recent hydrological evolution in the Duero Basin (Spain). *Regional Environmental Change*, 12(1), 17–33. <https://doi.org/10.1007/s10113-011-0236-7>
- Percival, D. B., & Walden, A. T. (2000). *Wavelet methods for time series analysis*. Cambridge University Press.
- Pérez-Ciria, T., Labat, D., & Chiogna, G. (2019). Detection and interpretation of recent and historical streamflow alterations caused by river damming and hydropower production in the Adige and Inn river basins using continuous, discrete and multiresolution wavelet analysis. *Journal of Hydrology*, 578, 124021. <https://doi.org/10.1016/j.jhydrol.2019.124021>
- Prieto, I., Armas, C., & Pugnaire, F. I. (2012). Water release through plant roots: New 764 insights into its consequences at the plant and ecosystem level. *New Phytologist*, 193(4), 830–841. <https://doi.org/10.1111/j.1469-8137.2011.04039.x>
- Probst, J. L., & Tardy, Y. (1987). Long range streamflow and world continental runoff fluctuations since the beginning of this century. *Journal of Hydrology*, 94(3–4), 289–311. [https://doi.org/10.1016/0022-1694\(87\)90057-6](https://doi.org/10.1016/0022-1694(87)90057-6)
- Restrepo, J. C., Ortiz, J. C., Pierini, J., Schrottke, K., Maza, M., Otero, L., & Aguirre, J. (2014). Freshwater discharge into the caribbean sea from the rivers of Northwestern south America (Colombia): Magnitude, variability and recent changes. *Journal of Hydrology*, 509, 266–281. <https://doi.org/10.1016/j.jhydrol.2013.11.045>
- Schleiss, A. J., Franca, M. J., Juez, C., & De Cesare, G. (2016). Reservoir sedimentation. *Journal of Hydraulic Research*, 54(6), 595–614. <https://doi.org/10.1080/00221686.2016.1225320>
- Şen, Z. (2021). Reservoirs for water supply under climate change impact—A review. *Water Resources Management*, 35(11), 3827–3843. <https://doi.org/10.1007/s11269-021-02925-0>

- Teuling, A. J., De Badts, E. A., Jansen, F. A., Fuchs, R., Buitink, J., Hoek van Dijke, A. J., & Sterling, S. M. (2019). Climate change, reforestation/afforestation, and urbanization impacts on evapotranspiration and streamflow in Europe. *Hydrology and Earth System Sciences*, 23(9), 3631–3652. <https://doi.org/10.5194/hess-23-3631-2019>
- Tiwari, M. K., & Adamowski, J. (2013). Urban water demand forecasting and uncertainty assessment using ensemble wavelet-bootstrap-neural network models. *Water Resources Research*, 49(10), 6486–6507. <https://doi.org/10.1002/wrcr.20517>
- Torrence, C., & Compo, G. P. (1998). A practical Guide to wavelet analysis. *Bulletin of the American Meteorological Society*, 79(1), 61–78. [https://doi.org/10.1175/1520-0477\(1998\)079<0061:apgtwa>2.0.co;2](https://doi.org/10.1175/1520-0477(1998)079<0061:apgtwa>2.0.co;2)
- Trigo, R. M., Osborn, T. J., & Corte-Real, J. M. (2002). The North Atlantic oscillation influence on Europe: Climate impacts and associated physical mechanisms. *Climate Research*, 20(1), 9–17. <https://doi.org/10.3354/cr020009>
- Trigo, R. M., Pozo-Vázquez, D., Osborn, T. J., Castro-Díez, Y., Gámiz-Fortis, S., & Esteban-Parra, M. J. (2004). North Atlantic oscillation influence on precipitation, river flow and water resources in the Iberian Peninsula. *International Journal of Climatology*, 24(8), 925–944. <https://doi.org/10.1002/joc.1048>
- Vicente-Serrano, S. M., Beguería, S., & Lasanta, T. (2006). Diversidad espacial de la actividad vegetal en el Pirineo central español: Análisis de los procesos de sucesión mediante imágenes Landsat (1984–2001). *Pirineos*, 161, 59–84.
- Vicente-Serrano, S. M., Beguería, S., & López-Moreno, J. I. (2010). A multiscalar drought index sensitive to global warming: The standardized precipitation evapotranspiration index. *Journal of Climate*, 23(7), 1696–1718. <https://doi.org/10.1175/2009jcli2909.1>
- Vicente-Serrano, S. M., Domínguez-Castro, F., Murphy, C., Peña-Angulo, D., Tomas-Burguera, M., Noguera, I., et al. (2021). Increased vegetation in mountainous headwaters amplifies water stress during dry periods. *Geophysical Research Letters*, 48(18), e2021GL094672. <https://doi.org/10.1029/2021gl094672>
- Vicente-Serrano, S. M., McVicar, T. R., Miralles, D. G., Yang, Y., & Tomas-Burguera, M. (2020). Unraveling the influence of atmospheric evaporative demand on drought and its response to climate change. *WIREs Climate Change*, 11(2), e632. <https://doi.org/10.1002/wcc.632>
- Vicente-Serrano, S. M., Peña-Gallardo, M., Hannaford, J., Murphy, C., Lorenzo-Lacruz, J., Domínguez-Castro, F., et al. (2019). Climate, irrigation, and land cover change explain streamflow trends in countries bordering the northeast Atlantic. *Geophysical Research Letters*, 46(19), 10821–10833. <https://doi.org/10.1029/2019gl084084>
- Vicente-Serrano, S. M., Tomas-Burguera, M., Beguería, S., Reig, F., Latorre, B., Peña-Gallardo, M., et al. (2017). A high resolution data set of drought indices for Spain. *Data*, 2(3), 22. <https://doi.org/10.3390/data2030022>
- Williams, C. A., & Albertson, J. D. (2005). Contrasting short-and long-timescale effects of vegetation dynamics on water and carbon fluxes in water-limited ecosystems. *Water Resources Research*, 41(6), W06005. <https://doi.org/10.1029/2004wr003750>
- Wriedt, G., Van der Velde, M., Aloe, A., & Bouraoui, F. (2009). Estimating irrigation water requirements in Europe. *Journal of Hydrology*, 373(3–4), 527–544. <https://doi.org/10.1016/j.jhydrol.2009.05.018>
- Yin, X. A., Yang, Z. F., & Petts, G. E. (2011). Reservoir operating rules to sustain environmental flows in regulated rivers. *Water Resources Research*, 47(8), W08509. <https://doi.org/10.1029/2010wr009991>
- Yue, S., Pilon, P., Phinney, B., & Cavadias, G. (2002). The influence of autocorrelation on the ability to detect trend in hydrological series. *Hydrological Processes*, 16(9), 1807–1829. <https://doi.org/10.1002/hyp.1095>
- Zhang, Q., Singh, V. P., Sun, P., Chen, X., Zhang, Z., & Li, J. (2011). Precipitation and streamflow changes in China: Changing patterns, causes and implications. *Journal of Hydrology*, 410(3–4), 204–216. <https://doi.org/10.1016/j.jhydrol.2011.09.017>